Optical Spatial Heterodyned Interferometry for Applications in Semiconductor Inspection and Metrology

Kenneth W. Tobin* and Philip R. Bingham
Oak Ridge National Laboratory†, Oak Ridge, Tennessee, USA 37831 USA

ABSTRACT

Interferometric imaging has the potential to extend the usefulness of optical microscopes by encoding small phase shifts that reveal information about topology and materials. At the Oak Ridge National Laboratory (ORNL), we have developed an optical Spatial Heterodyne Interferometry (SHI) method that captures reflection or transmission images containing both phase and amplitude information at a high rate of speed. By measuring the phase of a wavefront reflected off or transmitted through a surface, the relative surface heights and some materials properties can be determined. In this paper we briefly review a variety of application areas where this technology has been applied including semiconductor wafer inspection, photolithographic mask metrology and inspection, and we conclude with a discussion regarding future work to apply SHI to MEMS device characterization.

Keywords: Spatial Heterodyned Interferometry, holography, semiconductor wafer inspection, photolithographic mask metrology, MEMS characterization

1. INTRODUCTION

Interferometric imaging has the potential to extend the usefulness of optical microscopes by encoding small phase shifts that reveal information about topology and materials. At the Oak Ridge National Laboratory (ORNL), we have developed an optical Spatial Heterodyne Interferometry (SHI) technology that captures reflection or transmission images containing both phase and amplitude information at a high rate of speed [1]. The method has also been described by us as Direct-to-Digital Holography (DDH) due to the similarity of the image formation model of the SHI system to the wavefront reconstruction process proposed by Dennis Gabor in 1948 known as holography [2]. By measuring the phase of a wavefront reflected off or transmitted through a surface, the relative surface heights and some materials properties can be determined. For our system the interferogram, or hologram, is formed directly on the surface of a CCD sensor and digitized.

For example, new advances in the production of photolithographic masks are enabling useful extensions of optical lithography techniques into the 90nm node and beyond [3]. With these new materials and formats come new issues related to mask inspection and metrology that must be addressed to guarantee adequate availability and function of these critical optical elements. SHI of phase shift masks (PSM) allows metrology [4] and detection of phase shift structures and defects [5]. Figure 1 shows phase image examples of transmission and reflection measurements of a PSM using our SHI system with 532nm interrogation wavelength. The alternating aperture phase shift mask (AAPSM) in this example has 0^o and 180^o induced shifts in conjunction with opaque chrome regions. Direct metrology of these phase shifts are possible with SHI systems.

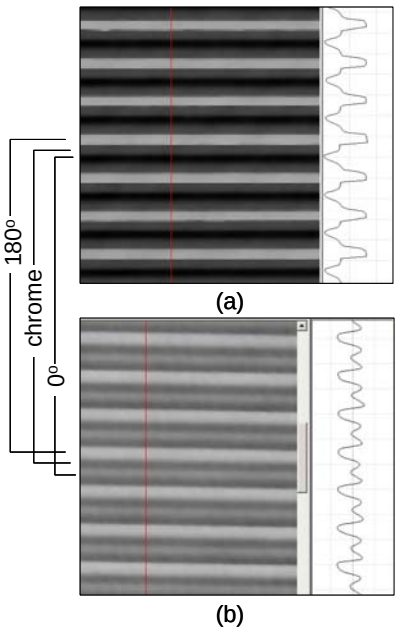

Figure 1 - Example of a reflectance (a) and transmission (b) measurement image of an AAPSM using the SHI technique.

* tobinkwjr@ornl.gov; phone 865.574.8521; fax 865.576.8380, http://www.ornl.gov/sci/ismv
† Prepared by Oak Ridge National Laboratory, managed by UT-Battelle, LLC, for the U.S. Department of Energy under Contract No. DE-AC05-00OR22725.

Applications of the SHI technology have been investigated for characterizing deep structures on semiconductor wafers (e.g., contacts, vias, and trenches) and for performing inspection and metrology on PSMs. In this paper we will describe the state of the SHI research that is ongoing at ORNL with regards to both reflection and transmission measurements on semiconductor wafer structures and on PSMs. We conclude by discussing one of our future directions for the application of this technology, which is to the characterization of the active motion elements of MEMS devices.

1.1. Background

SHI is a technique that captures an interferogram which is then passed through a reconstruction algorithm to produce the phase and amplitude of the captured wavefront. Figure 2 shows the basic layout of the reflective SHI system at ORNL. An illumination beam is emitted by the laser, which is then split into a reference and target arm path. The target arm path reflects the illumination beam off the object to be imaged while the reference beam is reflected off the mirror to produce a flat reference image. The two wavefronts (target and reference) are then mixed on the surface of an imaging device (CCD Camera) with a small angle between the two beam paths. This small angle produces a spatial heterodyne frequency. Various lenses are used to provide the proper magnification and acousto-optic modulators (AOMs) are used for shuttering and power balancing between the two arms.

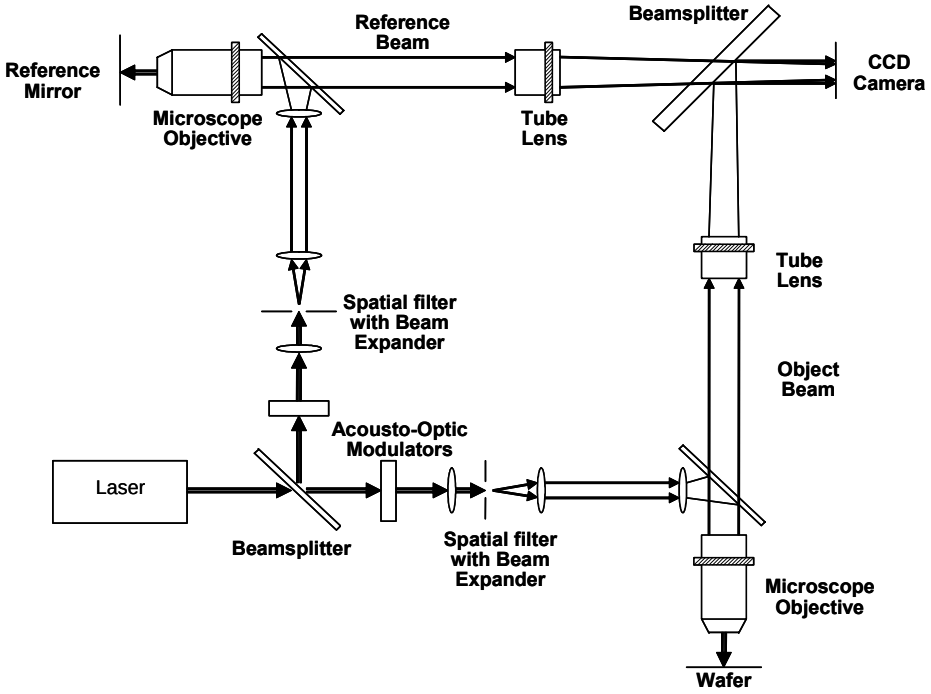

Figure 2 – Schematic representation of the reflective SHI system. The interferogram recorded on the CCD camera encodes the disparity in optical paths between the reference mirror and the target structure (labeled "wafer" in this case).

Forming an interference between the reference and target arms at a small angle introduces a phase wedge between the two beams. This phase wedge develops a linear fringe pattern across the image as seen in Figure 3 (a) and (b). To show this mathematically, SHI image formation can be adequately described using scalar diffraction theory [2], where the reference wavefront, $U_o(x,y)$, having amplitude, $A_0(x,y)$, and phase, $\phi(x,y)$, and the measurement wavefront, $U_M(x,y)$, having amplitude, $A_M(x,y)$, and phase, $\psi(x,y)$, , are described as,

$$U_o(x,y) = A_o(x,y)\, e^{-j\varphi(x,y)} \quad and \quad U_M(x,y) = A_M(x,y)\, e^{-j\psi(x,y)}$$

The intensity of the sum of these two wavefronts, $I(x,y) = |U_o(x,y)+U_M(x,y)|^2$, is recorded, e.g., on a photographic film media or in our case directly on the surface of a CCD camera, and is expressed as,

$$I(x,y) = \left|A_o(x,y)\right|^2 + \left|A_M(x,y)\right|^2 + 2\,A_o(x,y)\,A_M(x,y)\cos\left(\psi(x,y) - \phi(x,y)\right) \quad ,$$

which contains information not only regarding the intensity of the two waves, but also the relative phase between them at every spatial location *(x,y)*. In SHI, the reference wavefront is considered to have uniform amplitude and phase over the entire wavefront. However, the two beams are mixed at an angle. In the mathematics, we can treat this angle as a wedge on the reference wavefront with slopes in the *x* and *y* directions proportional to ω_x and ω_y such that $\phi(x,y) = 2\pi(\omega_x x + \omega_y y)$. As a simplification, we assume that the reference amplitude is equal to 1 and the baseline reference phase is 0° resulting in,

$$I(x,y) = 1 + \left|A_M(x,y)\right|^2 + 2A_M(x,y)\cos\left[2\pi\left(\omega_x x + \omega_y y\right) - \psi(x,y)\right]$$

The frequency constants, (ω_x, ω_y), represent the spatial heterodyne frequency of the system. With this in mind, the diagonal fringes shown in Figure 3 (b) represent the spatial carrier frequency (ω_x, ω_y) and fluctuations in the fringe intensity and position encode the amplitude and phase of the measurement wavefront respectively. Fourier frequency analysis is then used to isolate the carrier frequency information from the autocorrelation and reconstruct the phase and amplitude of the measurement wavefront [6]. Figure 3 (c) shows the frequency domain image resulting from a Fourier transformation of Figure 3 (a). This demonstrates the separability of the image on the carrier frequency from the autocorrelation image in the central portion of the spectrum.

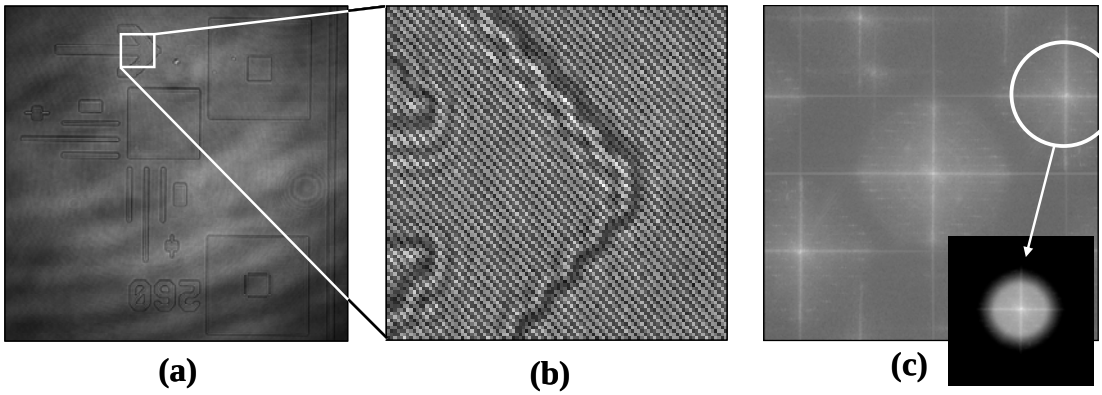

Figure 3 – Example of an interferogram of a chrome-on-chrome target in (a) showing the linear fringe patterns of an expanded region in (b). (c) shows the magnitude Fourier transform of (a) and the spatially heterodyned sideband response around the carrier frequency, (ω_x, ω_y). The inset in (c) shows the filtered sideband component whose inverse Fourier transform approximates the complex optical wavefront.

Fourier analysis is implemented as follows, where the sideband component is shifted to the center of the image and subsequently filtered with a suitable window function, W_B,

$$\Im\{U_F(x,y)\} = \Im\left\{\left[1 + A_M{}^2 + 2A_M\cos\left(2\pi\left(\omega_x x + \omega_y y\right) + \phi\right)\right]\cdot e^{-j2\pi(\omega_x x + \omega_y y)}\right\}\cdot W_B = \Im\{2A(x,y)e^{j\phi(x,y)}\}$$

The result of Fourier analysis (i.e., the inverse Fourier transform of the expression above) is the approximate determination of the original complex wavefront reflected from the target object, i.e.,

$$U_F(x,y) = 2A_M(x,y)\,e^{-j\psi(x,y)} \approx U_M(x,y)$$

Once an estimate of the original complex wavefront, $U_F(x,y)$, has been determined, the amplitude and phase are readily determined by,

$$A_M(x,y) = \sqrt{\mathrm{Re}\left\{U_F(x,y)\right\}^2 + \mathrm{Im}\left\{U_F(x,y)\right\}^2} \quad \textit{and} \quad \psi(x,y) = \tan^{-1}\left(\frac{\mathrm{Re}\left\{U_F(x,y)\right\}}{\mathrm{Im}\left\{U_F(x,y)\right\}}\right) \quad ,$$

where Re{} and Im{} represent the real and imaginary components of $U_F(x,y)$ respectively. Figure 4 (a) shows a 3-dimensional visualization of the resultant phase of the chrome-on-chrome target imaged by the SHI image shown in Figure 3. Figure 4 (b) and (c) show the phase map and corresponding 3-dimensional visualization of a target region on a semiconductor device.

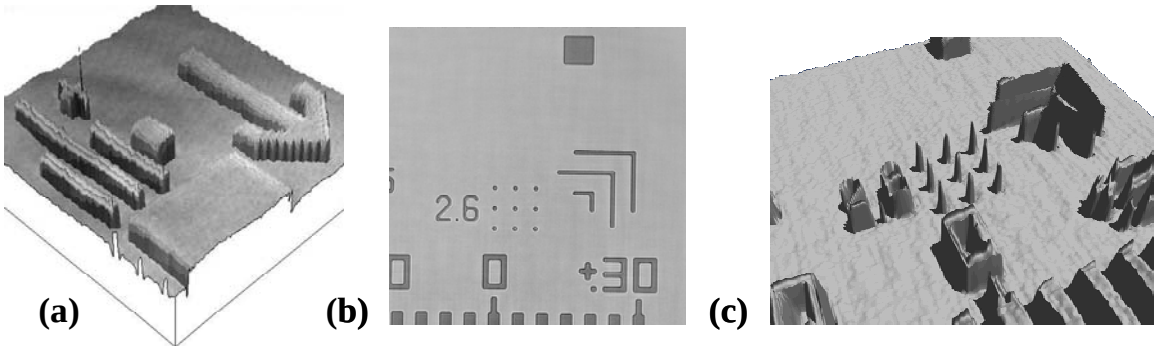

Figure 4 – (a) Visualization of 3-dimensional phase map determined from the chrome-on-chrome target in Figure 3. (b) Phase map developed from the alignment region of a semiconductor device pattern and in (c), the corresponding 3-dimensional visualization of the surface.

2. SEMICONDUCTOR WAFER INSPECTION

A critical need for semiconductor wafer fabrication is the high-aspect-ratio inspection (HARI) of structures such as contacts, vias, and deep trenches. A common HARI structure is the via which is used to electrically form connections between layers of the wafer. If a via is partially filled with photoresist or some other residue or contamination prior to being filled with a conductor (such as aluminum or copper), the connection is not made and often produces a killer defect rendering the device useless. Intensity imaging systems have difficulty finding a partially filled via due to the poor contrast between materials, but the phase portion of the complex wavefront captured by reflective SHI contains surface topology information that provides a stronger signal for detection of the partially filled via. Figure 5 show a phase image taken with the 532nm SHI tool of a test wafer containing an array of 220nm diameter vias that are 1,500nm deep and are spaced in a grid with a 540nm pitch. Within this grid is a single partially filled via with approximately 50nm of material in the bottom. While this partially filled via has a diameter that is smaller than half the illumination wavelength, the via still produces a strong signal difference due to the depth and material variation between the partially filled via and the other vias in the array.

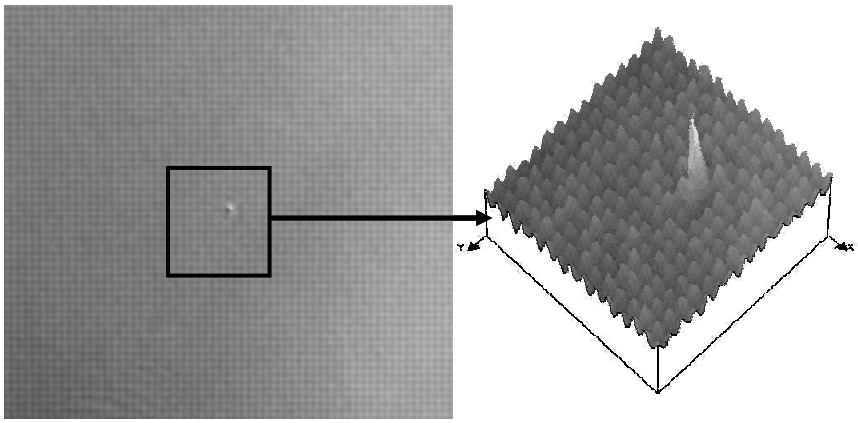

Figure 5 - SHI phase image of via array with single partially filled via in center (left). A 3-dimensional visualization of the phase surface (right) for the inset region.

There are several common methods available to perform automatic detection of defects on an industrial product such as a semiconductor wafer. These include comparison of the product to a CAD or other design file and comparison to a golden template that is typically composed of a defect-free image of the region to be inspected. A third method known as die-to-die comparison is the method we have chosen for defect detection and is outlined in Figure 6. Die-to-die comparison takes advantage of the fact that semiconductor wafers contain many copies of the same integrated circuit (IC). It is also useful since process variations (e.g., in film thickness) between spatially close die are small. Figure 6 shows the amplitude and phase images from a single die being compared to each of the two neighboring die. For SHI

we perform a direct comparison (i.e., subtraction) of the complex object wavefront. Other methods could include comparing the amplitude and phase separately, but a combined approach allows us to ignore issues with phase wrapping since it is not required that we directly determine the phase. The result is a comparison technique that comprehends both the phase and amplitude in a single method. Detected defects are assigned to the proper die based on whether the defect appears in each difference image, the first difference image, or the second difference image.

An example of defect detection using reflective SHI with 532nm illumination is given in Figure 7. This example demonstrates defect detection on a wafer with an intentional defect pattern within a memory structure. The defects are placed in a single cell within a die allowing comparison to neighboring cells in a die-to-die fashion. The design rule for this example is 350nm with the defect pattern identified in the upper right portion of the image. While the defects vary by type (e.g., bridge, void, orientation, position) on each row, the defect sizes are labeled as 100% (350nm), 50% (175nm), and 25% (87.5nm) meaning that at least one dimension of the defect is that percentage of the design rule. On the top row of the figure, the magnitude difference image between dies (A, B), and (B, C) are shown where the intentional defects are all located in die B. Below each difference is an image resulting from the application of a threshold to the difference image above. An image showing defects assigned to die B is given in the bottom right corner of the figure and is created by identifying all defects that appear in both threshold-difference images through a logical AND operation. From this image, it is noted that all of the 100% defects were detected, 86% of the 50% defects were detected and several of the 25% defects were detected. It is apparent that the SHI technique, which accounts for both phase and amplitude characteristics of the imaged surface, is very sensitive to defects that are small compared to the in-plane resolution of the microscope (i.e., ~266nm for this system). Further discussion of the application of SHI to semiconductor wafer inspection is available in references [7, 8].

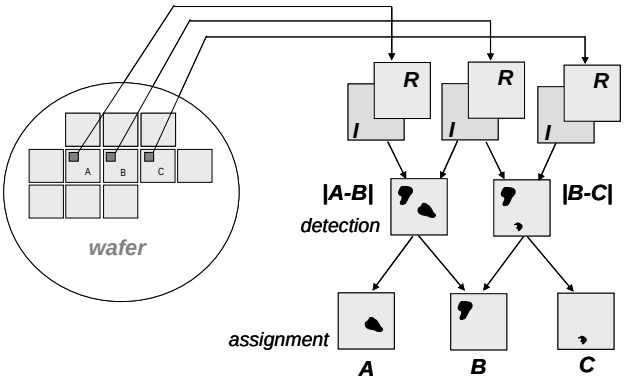

Figure 6 – Representation of the die-to-die detection procedure. Each neighboring die image is aligned and compared through subtraction. The defect is assigned to a die through simple logic.

3. PHOTOLITHOGRAPHIC MASK METROLOGY

The ability to perform accurate mask metrology is a requirement of lithographic technology for the control of mask patterning processes. At the 130nm technology node specified in the International Technology Roadmap for Semiconductors (ITRS), the minimum printed feature dimension on the wafer is 100nm with a corresponding minimum mask feature size of 100nm and 400nm for a 1X and 4X magnifications respectively. The ability to perform mask metrology in a cost-effective, high-throughput environment is becoming difficult to achieve with optical technology, even as microscopy systems reach into the deep ultra-violet (DUV) to achieve higher resolution. While scanning electron microscopy (SEM) systems provide the highest potential resolution for semiconductor metrology today, the high-cost, high-maintenance, vacuum operating environment, and potential for damage to the interrogated structure make them difficult to adapt to low-cost, high-throughput mask measurements. For these reasons we are looking to extend the application of SHI to the characterization of photomasks.

For mask metrology our goal is to make a determination of the absolute width and depth of printed lines, determine the roughness or shape of these lines, and perhaps most importantly, to measure the phase shifting properties of the mask that result either from the removal of material from the transparent regions of the mask or from the addition of phase-shifting materials to the surface of the mask. The SHI method is well suited to make robust and repeatable measurements of surface structure and phase shifting materials in a manner that has advantages over common techniques used today such as incoherent optical microscopy and scanning electron microscopy.

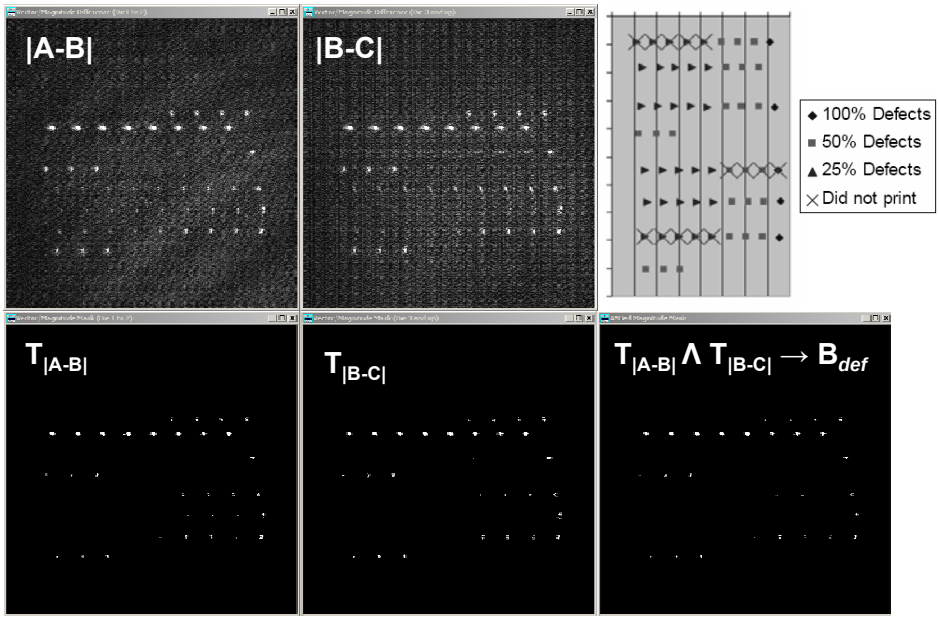

Figure 7 – Example of defect detection on a wafer containing programmed defects of varying size and shape. The top row shows the magnitude difference between dies (A,B) and (B,C). The bottom row shows detection after setting a suitable threshold. A simple logical AND process reveals the defects to be in die B.

Figure 8 shows schematically several of the challenges and advantages associated with mask measurements using SHI. In the figure, a reference wave, $U_o(x,y)$ is shown impinging on the surface of the mask. This wave is simultaneously reflected from, $U_R(x,y)$, and transmitted through, $U_T(x,y)$, the mask. The mask surface topology and material properties cause a modulation of the wavefront that is encapsulated both in the amplitudes, $A_R(x,y)$ and $A_T(x,y)$, and the phases, $\phi_R(x,y)$ and $\phi_T(x,y)$. Previous feasibility studies were limited to metrology with the reflected wavefront; however, development of a transmission system has enabled our study of the transmission response as well.

Advantages of operating in transmission mode include the ability to generate a strong signal from the phase-shifting and transparent regions of the mask in a similar fashion to the lithographic printing process. It should be noted that our ability to characterize the opaque regions of the mask are severely limited since no signal is received by the detector through these regions. In reflection mode the system characterizes the opaque (e.g., chrome) structures, yet reflects very little signal back towards the detector from the transparent regions of the mask. We have shown in the past that the reflected signal (i.e., about 4% of the incident illumination energy) is measurable from these transparent areas, while the opaque structures reflect a very strong signal [4].

The primary measurement enabled by the use of transmission SHI in mask metrology is the measurement of the phase shift through the mask. Thus, transmission provides a direct measure of the phase shifting regions of the mask. The phase measurement result will not match the designed mask phase shift unless the inspection wavelength matches the illumination, but the measurement can be easily scaled to effectively match the native mask wavelength

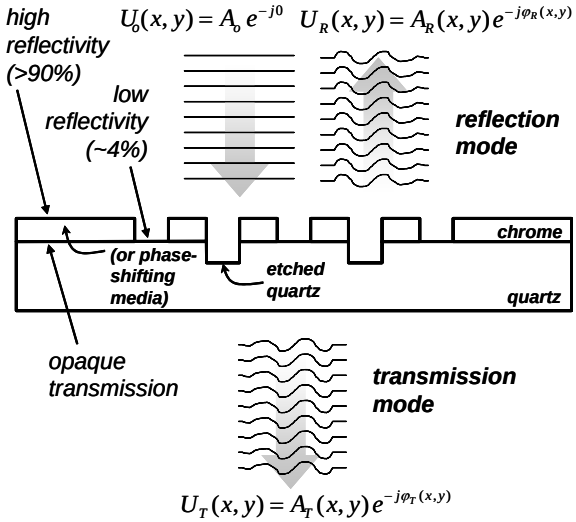

Figure 8 - Schematic representation of a reference wave interacting with a phase-shift mask in both reflective, $U_R(x,y)$, and transmissive, $U_T(x,y)$, modes.

according to the following expression,

$$\Delta\varphi = \Delta\varphi_{measured} \frac{\lambda_{measured}}{\lambda} \left(\frac{n-1}{n_{measured}-1} \right),$$

where $\Delta\phi$ is the effective measurement desired at the design wavelength for the mask while $\Delta\phi_{measured}$, $\lambda_{measured}$, and $n_{measured}$ correspond to the measurements obtained, for the phase difference and wavelength, and the index of refraction at the measurement wavelength.

Figure 9 shows an example of a transmission measurement of an AAPSM made with our modified SHI system. While transmission SHI allows direct measurement of phase through the mask, one challenge to performing these measurements is confusion in the phase image due to the opacity of the pattern. Since the amplitude of the wavefront is zero in the pattern regions, the phase response is meaningless and will produce a wide range of phase levels as seen to the left in Figure 9. To simplify metrology of the phase shift between the regions, a threshold is set on the amplitude image shown in the center of the figure to create a filter which is multiplied by the raw phase image to produce the image on the right. With this noise removed, automated algorithms can be applied to measure the phase shift differences between the lines in the filtered phase image.

While mask metrology is an important aspect of the mask characterization process in lithography, mask inspection is also critical. Mask defects occur by the addition or removal of unexpected materials to the mask during fabrication in a similar manner to wafer patterning. These defects in the mask can cause significant patterning issues when used for lithography because the phase-shift characteristics of the mask defect can be greatly accentuated during exposure, plus a mask defect will be repeated on every chip that is patterned during photolithography.

To test our SHI method for phase defect detection, we had access to a programmed phase defect mask that was well suited for analysis in our reflective system. A DuPont Photomask AAPSM designed for 248nm was used to test reflective SHI on phase defects [5]. This mask contained a variety of programmed phase defects in an array. The phase images of this mask is shown in Figure 10 for a variety of programmed defect categories.

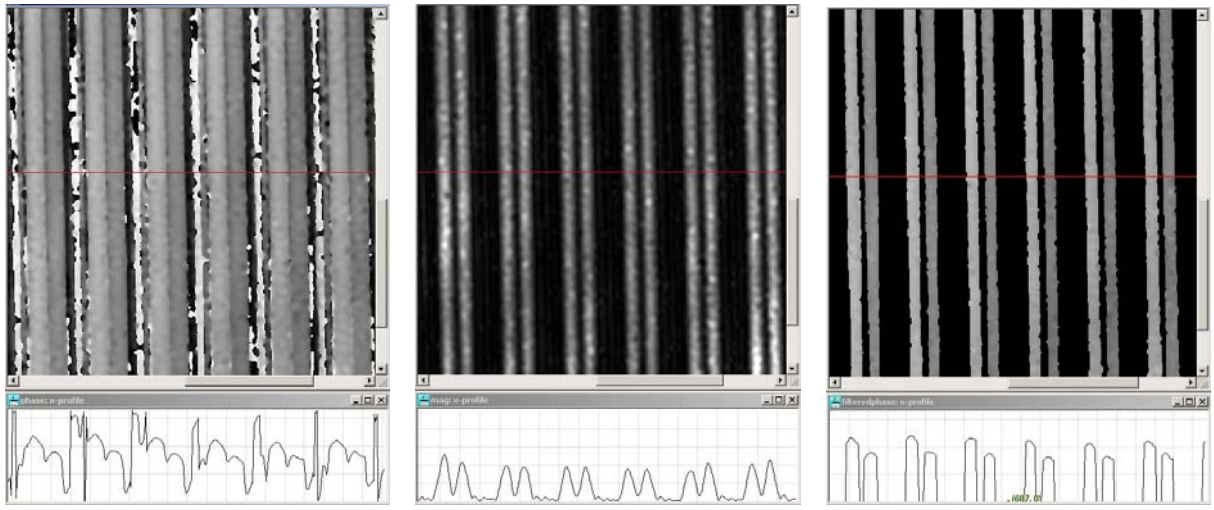

Figure 9 - Filtering of the transmission SHI phase response on an AAPSM pattern to ease phase measurement. (left) Phase response (middle) amplitude response, and (right) phase response filtered by amplitude.

The material around the edges and forming lines throughout each mask image is the pattern material. The phase shift regions on either side of each line can be seen as an alternating dark-light pattern indicating that the SHI tool is able to distinguish between the 0° and 180° phase shift regions used on the AAPSM. The mask features are 4× larger than the features that will be printed on the wafer, so the pattern lines are 520nm wide. Spaces (quartz regions) between the

lines are twice the line width or 1040nm. For each defect type and size, the pattern is printed multiple times to facilitate defect detection through die-to-die subtraction in a similar fashion to that described above for wafer inspection.

The SHI phase response for 60° phase defects on a 248nm mask using our 532nm illumination wavelength is ≈110°; the response for a 120° phase defect is ≈220°; and the response for a 180° phase defect is ≈330°. With phase subtraction, results actually fall between +180° and -180° so the responses for 60°, 120°, and 180° phase defects are 110°, -140°, and -30° respectively. Thus, we expect all three phase defect depths on the mask to be quite visible with our SHI system as is demonstrated in Figure 10.

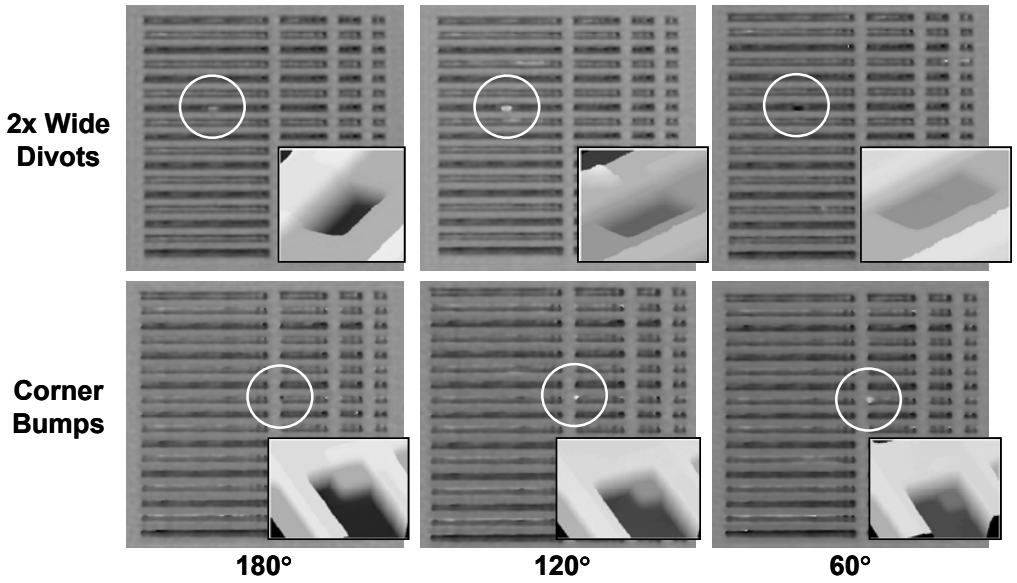

Figure 10 – Examples of a variety of phase defects detected by SHI imaging. Each main image was collected by reflection SHI while each corresponding inset is an AFM image of the programmed phase defect. The left-hand column represents 180° phase shift defects, the center 120°, and the right 60°.

4. FUTURE WORK

Our ongoing and future work to improve SHI performance relates to methods that can enhance the resolution of these systems as well as extend the gauge length of the measurement (i.e., reduce the complexities introduced by phase wrap ambiguities and errors in the SHI measurement). Micro Electro Mechanical Systems (MEMS) represent one area where enhanced SHI performance will be beneficial. Much of the success of the integrated circuit (IC) industry has been a result of inspection capabilities developed to monitor the wafer during production and product development. To similarly further the development of MEMS devices, MEMS-specific inspection systems are needed for both development and production. Many of the inspection modes used for ICs are not directly applicable to MEMS inspection due to the two main differences between IC and MEMS devices: mechanical motion and size. The mechanical motion (in and out of plane) of many MEMS devices requires inspection capabilities that can map this motion. Motion requires an inspection system capable of resolving topological differences and capturing information at a high rate of speed to stop motion. MEMS devices are typically much larger than IC devices in all three dimensions. Larger physical dimensions in-plane reduce the required resolution of the system and make inspection easier; however, the high aspect ratios caused by large out-of-plane structures introduce difficulties with phase wrapping for optical inspection techniques that typically use phase measurements to determine surface topology and with depth of focus for an optical system.

There are many categories of MEMS devices that are being built for a wide variety of applications today. Examples of these devices include microcantilevers for chemical detection, deformable mirror arrays for digital light processing, capacitive membrane devices for sensing acceleration or temperature, and micro machines that contain gears and

motors. Figure 11 shows a SEM image in (a) and SHI image in (b) of a triangular shaped microcantilever taken on the single wavelength, high-resolution SHI system developed by ORNL with an approximate depth of focus of 500nm. The SHI image reveals that the left portion of the cantilever is in focus, while the tip of the microcantilever has begun to blur due to the short depth-of-focus. This becomes clear based on the phase image in (c) which indicates that the cantilever height varies by four phase wraps, which is approximately equal to 1μm. Optical MEMS inspection systems have begun to incorporate methods for extending depth of focus using a combination of optical components and image processing techniques [9,10]. The issue of phase wrapping over such large out-of-plane distances persists in systems like ours if only a single wavelength is used to interrogate the range of motion of these mechanical structures.

To address the complexities associated with excessive phase wrapping in SHI images we have chosen an approach that effectively extends the gauge length of the system using two simultaneous illumination wavelengths. The result is a new "beat" wavelength, $\lambda_b = \lambda_2\lambda_1 / (\lambda_2-\lambda_1)$ that reduces the number of phase wraps that will occur over a given height.

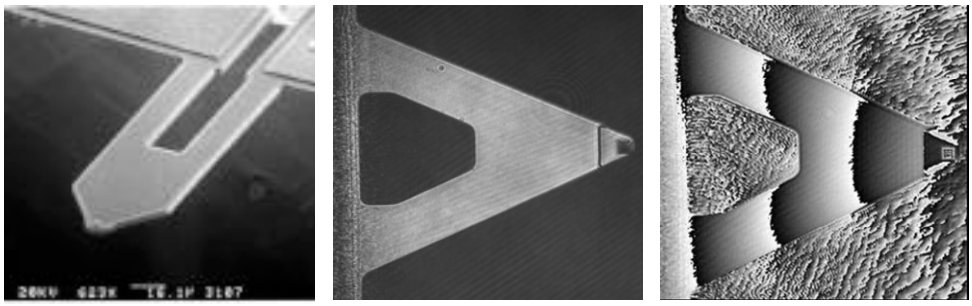

(a) **(b)** **(c)**

Figure 11 – Examples of a MEMs microcantilever device. (a) SEM image of a microcantilever showing typical geometry and attachment to the silicon structure. (b) Single wavelength SHI hologram of a microcantilever tip. (c) Single wavelength phase reconstruction showing wraps across tip indicating deflection.

The effect of this new beat wavelength, λ_b, is readily apparent when considering Figure 12 below. In this figure, we have imaged a section of a concave mirror with a radius of curvature of 53mm. In (a) and (b) the wavelength-independent phase results are shown for the 633nm and 612nm illumination wavelengths respectively. In (c) the resulting phase is shown when the two are beat together. In this case the new effective beat wavelength of 18.2μm results in a reduction in the number of phase wraps by a factor of 30 and an effective gauge length increase from ~ 300nm to 9μm. It is this type of enhancement in conjunction with our inherent ability to capture real-time (i.e., frame-rate) hologram data that makes (and will make) the SHI technology suitable for analysis of motion elements on MEMS.

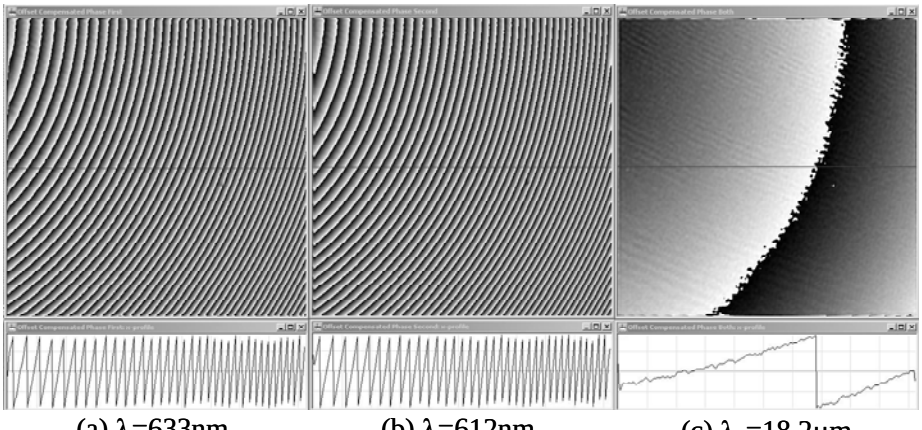

(a) λ=633nm (b) λ=612nm (c) λ_b=18.2μm

Figure 12 – Phase reconstruction of a section of a concave mirror with a radius of curvature of 53mm. (a) Phase at 633nm. (b) Phase image at 612nm. (c) Phase reconstruction as a result of beating the 633nm and 612nm signals together to give an effective beat wavelength of 18.2μm.

5. CONCLUSION

ORNL has been developing an SHI technology for semiconductor metrology and inspection applications since the mid-1990's. In this paper we have briefly reviewed the basic technology and theory underlying the directly digitized encoding of the image hologram on the face of the CCD sensor and the estimation of the complex optical wavefront from which object phase and amplitude are derived. This technology is being used in the commercial sector through a license agreement for the inspection of high-aspect-ratio features on printed semiconductor wafers and it is being investigated for application to photomask metrology. These applications with results were described herein. Finally we briefly discussed our future work directions to characterize the mechanical motion elements of MEMS devices.

6. ACKNOWLEDGEMENTS

We wish to acknowledge nLine Corporation of Austin, Texas, for their partnership and continued support of this research for semiconductor wafer inspection. We also wish to thank the National Institute of Standards and Technology for their financial support through the Advanced Technology Program (NIST-ATP). Finally we wish to thank SEMATECH of Austin, Texas, and its Member Companies for their continued support of this research, in particular to the investigation of the its applicability to photomask metrology.

7. REFERENCES

[1]. Thomas, C.E., et. al., "Direct To Digital Holography For High Aspect Ratio Inspection of Semiconductor Wafers", International Conference on Characterization and Metrology for ULSI Technology, NIST, Austin, TX, March 24-28, 2003.

[2] Goodman, J.W., Introduction to Fourier Optics, 2nd Ed., McGraw-Hill Companies, Inc., New York, New York, 1996, p. 295.

[3] International Technology Roadmap for Semiconductors (2004 Update), Semiconductor Industry Association and International SEMATECH, 2004.

[4] Bingham, P.R., Tobin, K.W, Bennett, M.H., Marmillion, P., "Preliminary Results for Mask Metrology Using Spatial Heterodyne Interferometry," 23rd BACUS Symposium on Photomask Technology, 8-12 September, Monterey Convention Center, Monterey, CA, 2003.

[5] Bingham, P.R., Tobin, K.W., Bennett, M.H., Marmillion, P., "Phase Defect Detection with Spatial Heterodyne Interferometry," Microlithography, Proceedings of the SPIE Vol. 5378, May 2004.

[6] E. Voelkl, L.F. Allard, D.C. Joy, Introduction to Electron Holography, Kluwer Academic Press / Plenum Publishers, New York, New York, 1999.

[7] Schulze, M.A., Hunt, M.A., Voelkl, E., Hickson, J.D., Usry, W., Smith, R.G., Bryant, R., and Thomas, C.E., "Semiconductor wafer defect detection using digital holography," Proceedings of the SPIE, Vol. 5041, pp. 183-193, 2003.

[8] Bourgeat, P., Meriaudeau, F., Tobin, K.W., Gorria, P., "Patterned Wafer Segmentation," SPIE Journal of Electronic Imaging, Vol. 13, No. 3, July 2004.

[9] Barton, D.L., Wairaven, J.A., Dowski, E.R. Jr., Danz, R., Faulstich, A., Faltermeier, B., "Wavefront Coded ® imaging systems for MEMS analysis," Proceedings of the 28th International Symposium for Testing and Failure Analysis, pp. 295-303, 2002.

[10] Dowski, E.R. Jr., Cathey, W.T., "Extended depth of field through wave-front coding," Applied Optics, Vol. 34, No. 11, pp. 1859-1866, 1995.